

Stabilization of the high-temperature and high-pressure cubic phase of ZnO by temperature-controlled milling

C. S. Tiwary¹ · D. Vishnu² · A. K. Kole² · J. Brahmanandam³ · D. R. Mahapatra³ · P. Kumbhakar² · K. Chattopadhyay¹

Received: 3 June 2015 / Accepted: 27 August 2015 / Published online: 15 September 2015
© Springer Science+Business Media New York 2015

Abstract The reversible transition of wurtzite to rock salt phase under pressure is well reported in literature. The cubic phase is unstable under ambient conditions both in the bulk and in nanoparticles. This paper reports defect-induced stabilization of cubic ZnO phase in sub 20 nm ZnO particles and explores their optical properties. The size reduction was achieved by ball milling in a specially designed mill which allows a control of the milling temperature. The process of synthesis involved both variation of milling temperature (including low temperature ~ 150 K) and impact pressure. We show that these have profound influence in the introduction of defects and stabilization of the cubic phase. A molecular dynamics simulation is presented to explain the observed results. The measured optical properties have further supported the observations of defect-induced stabilization of cubic ZnO and reduction in particle size.

Introduction

Nanoparticles of ZnO have potential applications in developing piezoelectric transducers, phosphors, transparent conducting film and in human skin protection by blocking ultraviolet light of the sun [1–3]. The piezoelectric properties are exhibited only by ZnO having wurtzite (WZ, P6₃mc) structure. The property is lost due to phase transformation to other structures under different loading conditions [1–6]. Till-to-date, variety of structures of ZnO have been reported in the literature that include WZ, zinc blende (ZB), rock salt (RS), layered structure (LY), hexagonal structure (HX) and body-centred tetragonal structure (BCT-4) [1–6]. Among all of these, WZ is the most stable phase of ZnO at room temperature and hence it is the commonly observed phase under ambient conditions. On the other hand, RS (Fm3m) and other phases can be obtained under specific growth conditions or under non-equilibrium conditions, such as at high temperature and pressure [4–6]. WZ phase shows high-quality n-type conductivity in ambient condition, whereas RS-cubic phase shows electronic structure with an indirect band gap that may be compatible for high p-type doping [3, 7]. The possibility to trap the high pressure phase at ambient condition would therefore be of great interest. However, the WZ to RS transition is reversible under ambient conditions. At room temperature, ~9 GPa applied pressure leads to a WZ to RS phase transition but transforms back to WZ phase on release of pressure. [8] In the last two decades, there are several interesting and detailed studies on the pressure-induced phase transformation in ZnO. These are further improved with help of recent theoretical calculation by Wang et al. [9]. The effect of size on transition pressure is also examined in recent reports [4–16]. The required pressure for phase transformation is related to unit

✉ C. S. Tiwary
cst.iisc@gmail.com

✉ K. Chattopadhyay
Kamanio@materials.iisc.ernet.in

¹ Department of Materials Engineering, Indian Institute of Science, Bangalore 560012, India

² Nanoscience Laboratory, Department of Physics, National Institute of Technology, Durgapur 713209, India

³ Department of Aerospace Engineering, Indian Institute of Science, Bangalore 560012, India

cell volume for nano-size and bulk ZnO. This can be described with help of Murnaghan equation of state (EOS) [4–16].

$$P = \frac{B_0}{B'_0} \left[\left(\frac{V_0}{V} \right)^{B'_0} - 1 \right] \quad (1)$$

In the Eq. (1), B_0 is the isothermal bulk modulus and B'_0 is its pressure derivative. The fitting of pressure volume data indicates the value of the latter to be equal to 4. The particle size reduction significantly affects the value of B_0 . For nano-size, the value is higher than that of the corresponding bulk material [4–16]. Hence, the pressure required for phase transition in nano-size ZnO is higher in comparison with that of bulk ZnO under normal conditions. Jiang et al. showed that particles of WZ–ZnO having 12 nm particle size transform to cubic phase at 15.6 GPa [15]. On decompression, only a small fraction of cubic phase is retained. Apart from size, the shape also plays a crucial role in these kinds of transformations [17–19]. The WZ ZnO nanorod undergoes transition at a pressure of 27 GPa [13]. This transformation shows a substantial phase hysteresis (transformation back to WZ phase) as a function of size. As a result, producing the cubic phase in normal processing condition is difficult. Therefore, the previous works are mostly limited to phase transformation studies under high pressure. In the current paper, we have used a specially designed ball mill (KC0) where temperature can be controlled up to 150 K under inert atmospheres [20–24]. In the process of producing nanocrystalline powder of large quantity using current mill, we expect powders with high defect density. In one of our recent works, we have shown that ball to powder ratio (BPR) plays a crucial role in ball milling process [23]. By increasing the BPR, we can increase the load applied on powder during impact. We have chosen a large BPR of 100:1 to generate high impact pressure and room temperature, and cryo-temperature milling has been performed in order to understand the effect of temperature and pressure. A detailed analysis illustrates the difference between these effects. Detailed MD simulation studies consider these effects and demonstrate its influence on phase transformation. The optical study of these materials explains the effect of the phase transformation. The studies on optical properties of these materials explain the effect of the phase transformation on the absorption and photoluminescence emission characteristics of the prepared materials.

Experimental details

The pure ZnO powder with 5–20 μm size (purity 99.8 %, supplied by Sigma Aldrich) is milled in our specially designed cryomill (KC0). The in-house developed mill is

capable of performing milling at room temperature as well as can be cooled down to LN_2 temperature. In KC0 mill, there is no interaction between coolants and sample. In addition, it's capable of milling under controlled atmosphere. In the present work Argon is used as atmosphere. The details about the mill are reported in elsewhere [11–15]. The ball to powder ration of 100:1 is used in the milling. The dry milling is performed in room temperature as well as liquid nitrogen cooled temperature (~ 150 K). Samples are collected in between time interval for analysis. Samples are kept in vacuum desiccators in order to avoid contamination and moisture.

The powders are characterized by X-ray diffraction technique using a Pan analytical Xpert Pro X-ray powder diffractometer with Cu $K\alpha$ radiation ($\lambda = 0.154056$ nm). The powder diffraction from 20° to 90° is performed with a step size of 0.008 and a scan speed of $0.2^\circ/\text{min}$. The crystallite sizes were calculated from peak broadenings (after separation of the contributions from strain and instrumental broadening). Electron Probe micro-analyser with a field emission gun (FEG-EMPA, JEOL) is used for composition analysis. The JEOL certified standard pure elements are used for calibration at 15 kV and 50 nA. The analysis was carried out for all elements from Boron to tungsten. For the preparation of TEM samples, the liquid solution is drop casted with help of micropipette on carbon-coated Cu mesh grids of 300 meshes. The TEM grid is then dried in GATAN PUMPING STATION (Model 655). A detailed TEM analysis has been performed with help of TEM (Technai F30) operating at 300 kV. The diffraction condition of the TEM is calibrated with help of gold standards. The TEM image processing and analysis is performed with help of Gatan digital microanalysis software.

Results and discussion

The XRD patterns shown in Fig. 1a reveal the presence of cubic peak in room temperature-milled sample after 2 h. Its relative intensity increases with milling duration and saturates to a maximum phase fraction of 40 % for 40 h of milling. The phase fraction is calculated using relative intensity ratio of the two peaks [23]. The crystallite size is calculated using Williamson-Hall (WH) methods, shown in Fig. 1b. The crystallite size decreases as milling duration increases. The structure of the phase and reduction of sizes are further confirmed using transmission electron microscope (TEM) (Technai F30, FEI operating at 300 kV). Figure 2a shows TEM micrograph from a sample milled at room temperature for 2 h revealing particle size of 20 ± 10 nm that consists of a mixture of hexagonal phase and cubic phase. The particle shows defect (inset of Fig. 2a(i)) and regions showing lattice

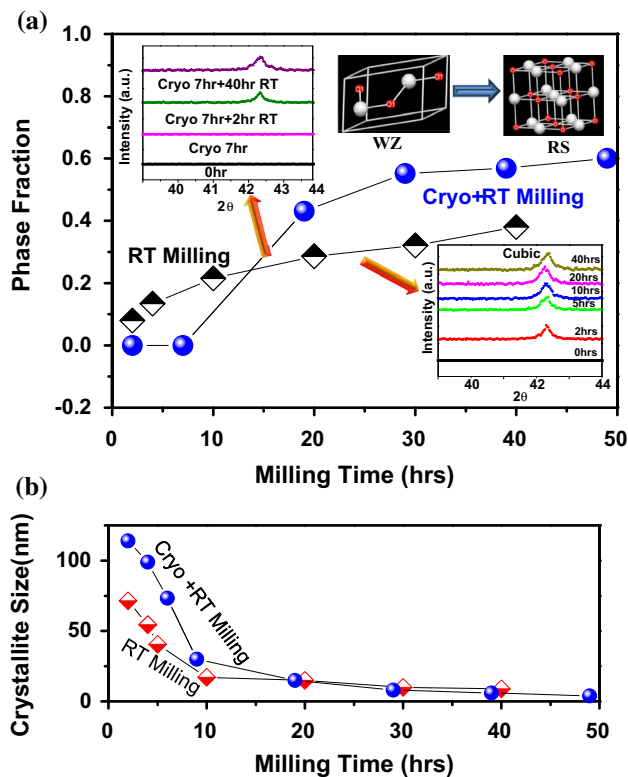


Fig. 1 **a** Fraction of WZ for different milling durations for RT and cryo + room temperature (RT). *Inset* shows XRD for both conditions; the *right top inset* shows unit cell of the two (WZ and RS) phases. **b** Variation of crystallite size as function of milling time for RT and cryo + RT

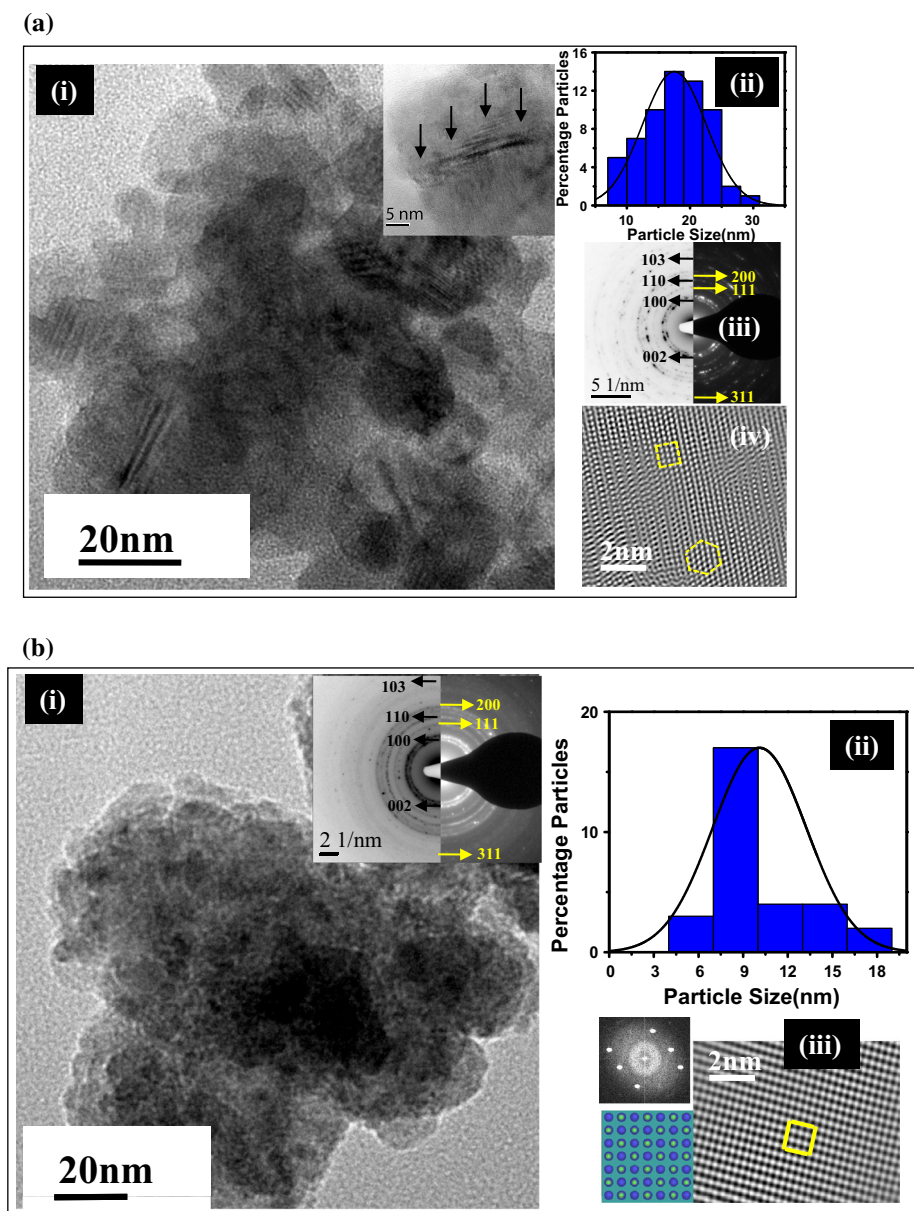
distortion (Fig. 2a(iv)). It further reveals that the transformation is nucleated and further driven by defects such as dislocation, shear band and twinning. The further milled (40 h) sample (Fig. 2b(i–iii)) reveals more intense cubic peaks and crystalline size of 9 ± 3 nm which are agglomerated. The diffraction pattern taken from an agglomerated particle using a bigger aperture clearly reveals intense diffraction ring of cubic phase. The HRTEM image shown in Fig. 2b(iii) further confirms the presence of cubic phase. The lattice spacing matches with cubic crystal structure that was generated through simulation using JEMS TEM software.

The above results show a possibility of retaining cubic phase at room temperature under normal condition. As the WZ to RS is a reversible process, the unloading process transforms the RS phase to WZ phase [4–19]. However, in current work, we have retained the cubic phase. This requires a clear understanding in terms of thermodynamic and kinetics. The phase transformation from WZ to cubic can be due to pressure, size, shape and temperature. In order to arrive at the actual reasons, we have first calculated pressure (P_{\max}) generated during ball milling. The application of load in a ball mill is very complex and it involves both axial and shear component. Depending on design of the mill, the loading conditions can vary that give

rise to variation in results in different ball mills. The insight of role played by both the components is summarized in a recent report [25–30]. As described in our previous work [23, 24], it is possible to estimate the impact pressure during the collision. A value of ~ 8.08 GPa was obtained for current milling conditions. However, the reported pressure required for transformation in bulk ZnO is 9 GPa. Apart from external pressure, we do expect an internal pressure due to Gibbs–Thomson effect given as $P_c = (2\gamma/r)$ [20, 29]. Assuming γ to be the average surface energy for hexagonal WZ phase (0.3 J/m^2), it gives an additional 1–2 GPa stress for a size of 10–100 nm. At the same time, it is well reported that as the size decreases, the pressure required for wurtzite to cubic transformation increases due to change in bulk modulus [4–25]. Thus, the influence of size and pressure to drive phase transformation is complex.

We now consider the effect of temperature on phase transformation. The temperature increases during ball milling. This can be determined as discussed in previous literature [20–25]. The temperature rise is estimated to be 425°C for current milling conditions. In order to understand the temperature effect on the samples during milling, the samples are cooled using LN_2 to 150 K during milling. No transformation can be observed even after 7 h of milling as shown by XRD data analyses, shown in Fig. 1a. Thus, the lowering of the temperature does not lead to the retentions of any transformed products. Further milling of the cryomilled sample at room temperature (i.e. in the absence of cooling) shows sharp increase of cubic phase fraction to 60 % and much smaller crystal of <20 nm size as shown in Fig. 1b. In order to understand the mechanism of transformation, a detailed TEM analysis has been performed (Fig. 3a–c). Figure 3a shows the TEM analysis of 2 h cryomilled sample. It shows a particle size of 120 ± 20 nm containing large defect density as shown in dark-field image in Fig. 3a(ii). The diffraction pattern shown in Fig. 3a(ii) reveals WZ phase. The high-magnification dark-field image shown in Fig. 3a(ii) reveals defected structure and shear band (shown with using black arrow) in a crystal. HRTEM image shown in Fig. 3a(iii) reveals these defects are mostly dislocation as marked in the figure. Further deformation at low temperature shows high density of defect with smaller particle size. Milling at room temperature of these cryomilled samples shows a large deformation or fragmentation that leads to a size of 12 ± 5 nm with a sudden increase in cubic phase fraction (Fig. 3b(i–iii)). The particles are well separated in this case. The HRTEM image (Fig. 3b(iii)) shows highly defected particles. The diffraction pattern taken using bigger aperture from a bigger particle shows the presence of cubic phase. Further increase in milling duration leads to decrease in size and increase in fraction of cubic phase as shown in Fig. 3c(i–iii). The well-separated particles are of

Fig. 2 **a(i)** Bright-field TEM image at low magnification with a high-magnification *bright-field* image as *inset* **(ii)** particle size distribution **(iii)** diffraction pattern covering large amount of particles **(iv)** high-resolution images showing the presence of defects in the sample for 2 h RT-milled sample. **b(i)** Bright-field TEM image at low magnification with diffraction pattern as *inset*. **(ii)** Particle size distribution **(iii)** High-resolution images showing the presence of cubic phase along with SAD pattern and generated lattice images for 40 h RT-milled sample



different shapes (Fig. 3c(vi)). The above microscopic study clearly reveals that the low temperature milling generates large defects in the particles although there is no phase transformation. The milling of the same sample further at room temperature gives rise to higher cubic phase fraction. The phase transformation at room temperature is already enhanced due to defect [31, 32]. The high defect density also leads to fracturing of the particle which gives rise to well-separated nanoparticles. Impurity is one of the major concerns in such kind of transformation in ball milling. In order to confirm the composition, we have analysed the ball milled powder using FEG-EPMA for all possible major impurities (iron, cobalt, Tungsten, etc.). The milled powders do not show any contamination. This is consistent with the similar results reported earlier [20, 24]. Although

the exact reasons need to be further explored, the decrease in adhesion and cold welding at low (cryo) temperatures can be identified as one of the possible reasons [20].

The cryomilling experiment clearly reveals that pressure and size alone cannot transform WZ into a cubic phase. An increase in temperature also plays a crucial role in phase transformation. There are several reports of decrease in required pressure (5.2 GPa) as a result of increase of temperature. Following the earlier reports, the relation between temperature and pressure can be given as [29, 33]

$$P(\text{GPa}) = A - B \times T(C), \tag{2}$$

where A and B are constants which are dependent on material properties. In the literature, the pressures required for WZ to RS transformation in bulk, 50, 20 and 10 nm

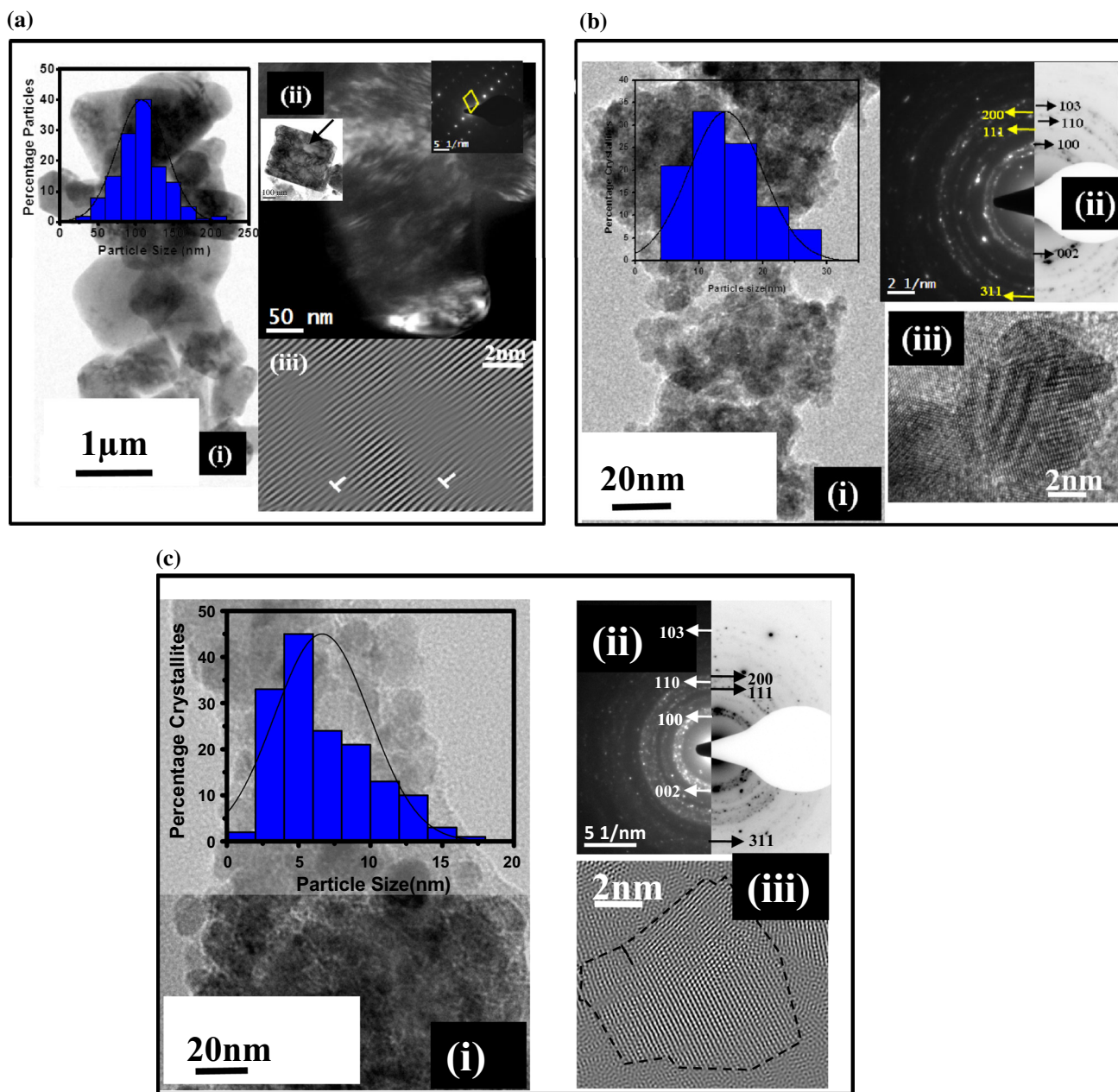


Fig. 3 **a(i)** Bright-field TEM image at low magnification and *inset* showing particle size distribution of ZnO 2 h cryomilled sample. **(ii)** Dark-field image at higher magnification, *right top inset* diffraction pattern from a single particle, *left top* particle showing shear band using *arrow* **(iii)** high-resolution image showing dislocation **b(i)** bright-field TEM image at low magnification and particle size

distribution **(ii)** diffraction pattern covering several particle **(iii)** HRTEM images of 7 h cryomilled followed by 2 h RT-milled sample. **c(i)** Bright-field image at low magnification and particle size distribution **(ii)** diffraction pattern **(iii)** HRTEM images of cryo + 40 h RT-milled samples

size ZnO nanoparticles are reported to be 9, 11, 13 and 15 GPa, respectively. On the other hand, the size (D) reduction gives rise to reduction in temperature (T_c) for transformation [23]. The required temperature decreases from 1700 °C for bulk to 1570, 1210, 900 °C for 50, 20 and 10 nm ZnO nanoparticles, respectively.

The irreversibility of RS phase in our case and the high RS phase fraction in combined milling as compared to

room temperature milling need further clarification. The pressure, temperature and size are not the only governing factors for phase transformation. The observed phenomena can be attributed to the large defect density generation during cryomilling. For the case of ZnS, Solozhenko et al. [8] have shown that the structural transformations are highly dependent on the nucleation of the second phase. The cryomilling gives rise to defects that can later acts as

nucleation sites for cubic phase. Observation of large fraction of cubic ZnO in our room temperature-milled samples following cryomilling is consistent with these conclusions. Unfortunately, however, no earlier report exists for defect-induced WZ–RS transformation in ZnO.

Hence, in order to understand the role of defects on the phase transformation of WZ to RS in normal condition and its retention after unloading, a detailed MD simulation has been performed. A simulation cell is constructed by repeating the ZnO unit cell in WZ phase in all directions. Periodic boundary conditions are used in all these directions to avoid the edge/surface effects. The inter-atomic interactions among atoms in the simulation cell are considered by the charge-optimized many-body (COMB) potential [33–36]. In this potential, the total energy E^T is the sum of all the atomic ionization energy E^{self} terms, the bond-order potential energy (E^{short}) with a dependency of charge, the Coulombic interaction energy (E^{Coul}) between the charged atoms, the polarization energy E^{polar} , the non-bonded atomic interaction energy E^{vdW} , the charge barrier energy E^{barr} and the angular dependent energy E^{corr} , which is given as [33–36]

$$E^T = \sum_i E_i^{\text{self}}(q_i) + \sum_i \sum_{j>i} \left(+ E_{ij}^{\text{short}}(r_{ij}, q_i, q_j) + E_{ij}^{\text{Coul}}(r_{ij}, q_i, q_j) + E_{ij}^{\text{polar}}(r_{ij}, q_i) + E_{ij}^{\text{vdW}}(r_{ij}) + E_{ij}^{\text{barr}}(q_i) + \sum_{k(\neq i,j)} E_{ij}^{\text{corr}}(r_{ij}, \theta_{jik}) \right), \tag{3}$$

where i, j and k are the atomic indices, q_i is the charge on atom i , r_{ij} is the distance of separation between the atoms i and j and θ_{ijk} is the angle subtending between atoms i, j and k . Charge on each atom is a variable which is identified by the electron negativity equalization using charge equilibration scheme which is based on a iterative calculation. This minimizes the charge on each atom in conjunction with the electron negativity of each atom. Details of the potential and mathematical expression are found in earlier report [33–36].

Atoms in the simulation cell with the defined inter-atomic potential are subjected to a compressive loading at a temperature of 300 K. The load is applied on the repeating cells by shrinking the simulation box in z direction. This is applied in successive increments with time, and at each stage of increment, the atomic lattice is relaxed to attain local energy minima. NVT simulations are carried out at each loading step with a time step of 0.5 fs. Such a choice of time stepping is advantageous in the optimization of atomic charges. At each loading step, charge equilibration scheme allows the atoms to dynamically vary the charge such that atomic interactions are accurately computed. In the loading process, atoms are adjusted to relax their

energy and change the phase of the simulation cell from WZ to RS. Phase transformation is identified with the help of radial distribution function (RDF) and its mathematical expression is given as [37]

$$g(r) = \frac{2V}{N^2} \left\langle \sum_i \sum_{i>j} \delta(r - r_{ij}) \right\rangle, \tag{4}$$

where N is the total number of atoms in the simulation cell considered, V is the volume of the simulation cell, r is the radius of sphere centred to each atom which is used to calculate the number of neighbours of that atom and delta function value is non-zero when the neighbouring atoms are within the sphere. The variation of $g(r)$ with respect to r shows several peaks which correspond to the first, second and third nearest neighbours and so on. Sum over delta function in $g(r)$ corresponds to the possible atomic pairs in the simulation cell. Once a clear shift in the RDF graph is detected, we start unloading (by releasing) the shrunk simulation box.

The stresses are calculated using the virial theorem considering the energy changes as well as changes in the

distance of separation between the atoms, which is given as [35]

$$\sigma_{\alpha\beta} = \frac{1}{V} \sum_i \sum_{i>j} \left(\frac{1}{2} \frac{\partial E^T}{\partial r_{ij}} \frac{\Delta r_{ij}^\alpha \Delta r_{ij}^\beta}{r_{ij}} - m_i v_i^\alpha v_j^\beta \right), \tag{5}$$

where m_i is the mass of each atom, v_i^α is the velocity of atom i in α direction and $\sigma_{\alpha\beta}$ is the stress in α direction when loading is in direction β . Δr_{ij}^α is the distance of separation between atoms i and j in α direction. First term in Eq. (5) represents the potential contribution to the atoms in the simulation box and the second term represents the kinetic contribution of atoms to the stress terms. The strain is measured as the ratio of the difference in the deformed length of the simulation box and its original length in the loading direction.

The stresses (σ_{zz}) are computed from the Eq. (5) and plotted with strain (ϵ_{zz}) in Fig. 4a. A gradual increase in σ_{zz} is observed due to the loading till ϵ_{zz} reaches to a value of 0.1. After this, the slope of the stress–strain curve changes and a drastic increase in the stress level is observed due to the change of orientation of the Zn–O bonds (as shown in atomic configurations A and B in Fig. 4c). Under a

compressive loading, the length of the Zn–O bonds starts decreasing, thereby increasing the bond energy because of the Coulombic and other charge-related contributions. As a result, the stress levels also increase. This leads to an unstable condition and the atoms start moving towards lateral directions (x and y) with respect to the loading direction (z) (directions are shown in inset of Fig. 4d), which causes a bending in the bond between the connecting atoms, highlighted in the atomic configurations. The relaxation time used in the simulation scheme helps to reduce the energy and finally changes the atomic configurations to a local energy minimum that corresponds to RS

phase of ZnO. WZ to RS phase transition can be seen clearly in the snapshots labelled as A and B (in Fig. 4c) and their stress levels are also marked in the stress–strain curve of Fig. 4a. RDF is calculated for atomic configurations at selective strain values and plotted in Fig. 4b. We have calculated RDF for atoms of similar type (i.e. Zn–Zn or O–O). Interestingly, the Zn–O bond length remains unchanged after the transformation. The first peak in the RDF plot corresponds to the first nearest neighbour atom position which is located at 0.32 nm for WZ phase and 0.28 nm for RS phase. The shift in the peak also clearly confirms WZ \rightarrow RS phase transformation.

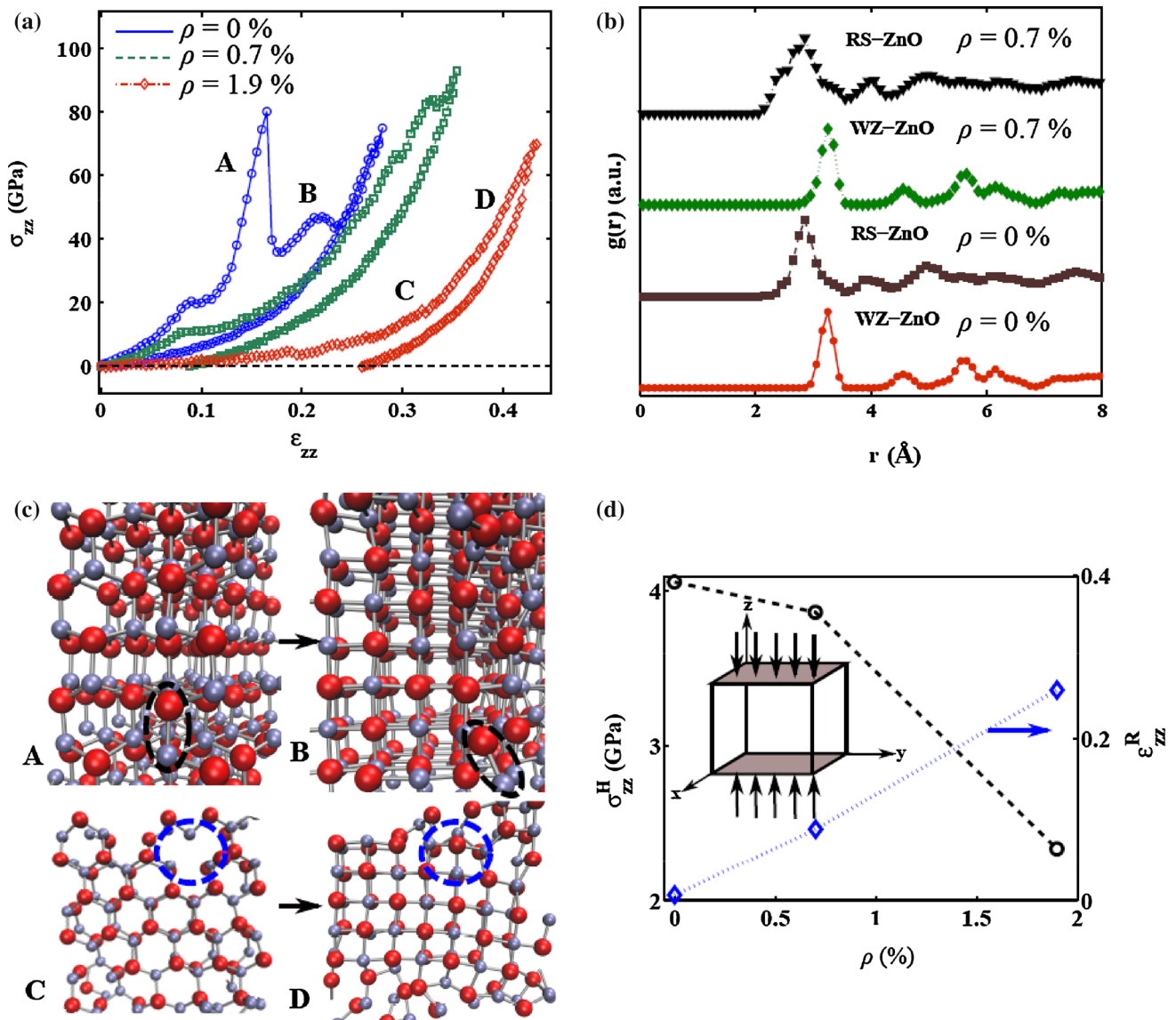


Fig. 4 **a** Computed stress–strain curves for ZnO with 0, 0.7 and 1.9 % defects. **b** Computed RDF variation with distance of separation for ZnO with 0 and 0.7 % defects. **c** Atomic configurations of ZnO with 0 and 1.9 % defects. A, B, C and D represent the atomic

snapshots at different locations of stress–strain curve. **d** Dependence of hysteresis area under stress–strain curve and the remnant strain with defect concentration

Under identical loading conditions, stress–strain curves for ZnO with increasing defects concentration (ρ) equal to 0.7 and 1.9 % are shown in Fig. 4a. The defects are created in the simulation cell by the removing atoms randomly, followed by stabilization. The defect concentration is defined as the ratio of number of atoms removed to the total size of the simulation cell. The total number of atoms in the simulation cell is about 1000. When ρ is equal to 0.7 %, 87 atoms are removed randomly from the simulation cell. In snapshot C of Fig. 4c, defect related to atom deficiency is highlighted. The stress values in defected ZnO crystals are much lower compared to pristine ($\rho = 0\%$) crystal. A careful observation of the atomic configurations indicates WZ to RS phase change but at very high stress levels. The transition process is enhanced due to migration of few atoms into defects. From the snapshots C and D in Fig. 4c, it can be clearly seen that oxygen atom initially located at the circumference of the marked dashed line moves to the centre and then gets bonded with the surrounding atoms which ultimately constitute RS phase. On further unloading, the simulation cell does not recover WZ phase. The simulation cell reaches to zero stress with a remnant strain (ϵ_{zz}^R) which indicates a partial recovery of the WZ phase from RS. RDF for defect concentration of 0.7 % is plotted in Fig. 4b, which also confirms this partial reversal of original phase (WZ). The remnant strain in the loading–unloading process is calculated for 0, 0.7 and 1.9 % defect concentrations. ϵ_{zz}^R increases with increase in ρ . Also, the hysteresis area (σ_{zz}^H) under the stress–strain curve decreases with increasing defect concentrations. Figure 4d indicates the variation of σ_{zz}^H and ϵ_{zz}^R with ρ . In the current work, we have considered point defects as a generic example to illustrate the role of defects, but in experimental results, we also observe the presence of dislocations and shear bands. It will be interesting to expand the size of the sample box and incorporate them and show the effect of these larger defect arrangements.

To summarize, the simulation shows that as the fraction of defect increases, the stress required for phase transformation decreases and it stabilizes high pressure and temperature phase. It reveals an interesting unexplored idea that introducing defects in ZnO helps in phase transformation. There are several other materials such as, ZnS, ZrO₂ and TiO₂, where doping introduces defects and stabilizes the unstable phases [37–40]. The current simulation and experiments can explain the mechanism of these experimental phenomena. The same can be extended for processing other unstable but useful oxides as well.

In order to further verify our observation related to defect and correlate phase transformation with its optical application, a detailed optical measurement has been performed. As discussed in introduction, the stability of cubic

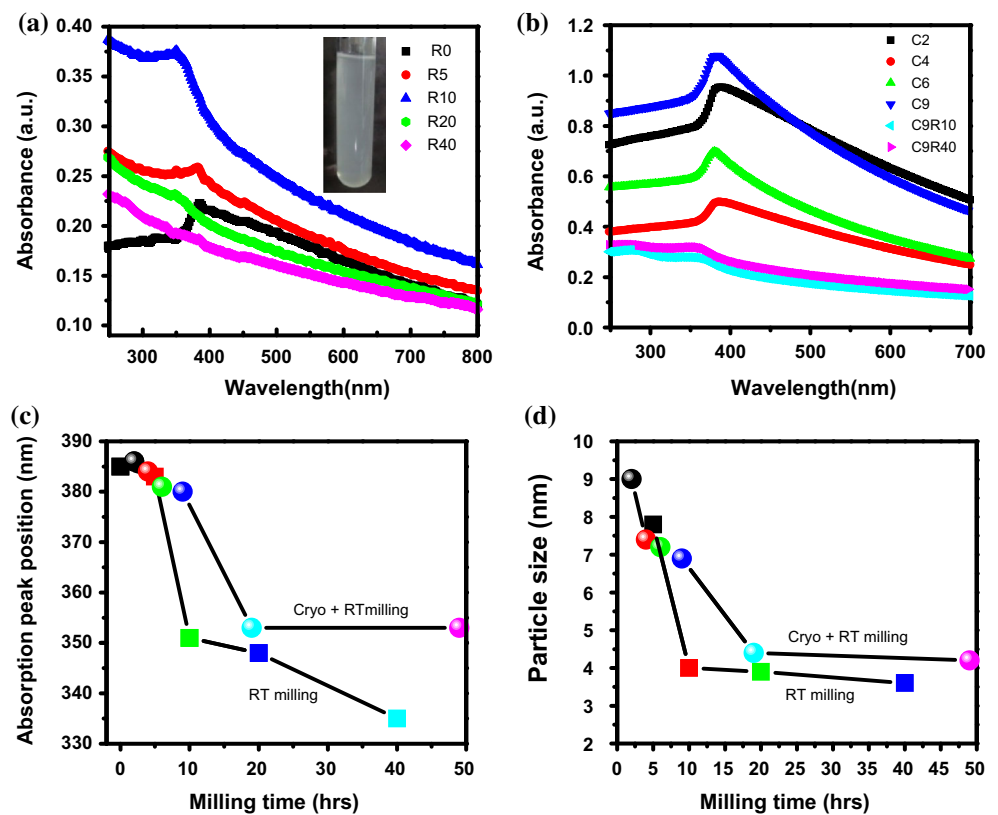
ZnO at normal condition is difficult, and hence, there is no report on its effect on optical properties. The UV–Vis absorption spectra of the samples have been measured at RT by dispersing them in deionised water followed by ultrasonication. Figure 5a, b shows the UV–Vis absorption spectra of the samples obtained by RT milling as well as RT milling following by cryomilling, respectively. The inset of Fig. 5a shows an aqueous dispersion of the sample obtained by 20 h RT milling. As can be seen from Fig. 5a, the starting material shows an absorption peak at 384 nm (3.23 eV) which is very close to the bandgap of 372 nm corresponding to bulk ZnO ($E_g = 3.34$ eV) [41]. It has been observed that with the increase in milling time, the absorption peak is blue shifted from 384 to 335 nm when the samples are milled for 40 h at RT. Similar blue shift can also be observed for the samples synthesized by cryomilling as well as by cryomilling followed by RT milling, shown in Fig. 5b.

Samples obtained from cryomilled sample reveal the presence of an additional peak at smaller wavelength (~ 272 nm). This suggests additional presence of very small particles. Similar absorption peak at ~ 264 nm (in addition to the band-edge absorption peak) has been observed in Mn-doped ZnO nanocups and is attributed to the presence of some smaller sized nanoparticles [41]. The band-edge absorption peak positions for both the cases are shown in Fig. 5c, and these observed blue shift indicates that as the milling time increases, mean particle size decreases in conformity with the TEM observation discussed earlier. The particle sizes can be calculated from the UV–Vis absorption spectra by using the following Equation [42]:

$$r_{\text{NP}}(\text{nm}) = \frac{-0.3049 + \left(-26.23012 + 10240.72\lambda_p^{-1}\right)^{+1/2}}{-6.3829 + 2483.2\lambda_p^{-1}}, \quad (6)$$

where r_{NP} is the radius of the nanoparticles in nm and λ_p is the peak absorbance wavelength in nm. By Eq. (6), it has been found that the particle size decreases from ~ 7.8 to 3.6 nm when milling time increases from 5 to 40 h at room temperature and ~ 9.0 to 4.2 nm when the milling time increases from 2 to 40 h at cryomilling. The variation in particle size with increasing milling time is shown in Fig. 5d. The estimated average particle size from UV–Vis absorption spectra for RT-milled samples is smaller than that calculated from TEM analyses. The observed difference may be due to coarsening or sintering of smaller crystallites leading to the formation of larger particles during RT milling. On the other hand for cryomilled sample, these are well separated; hence, their size measurement matches with calculated ones within experimental error.

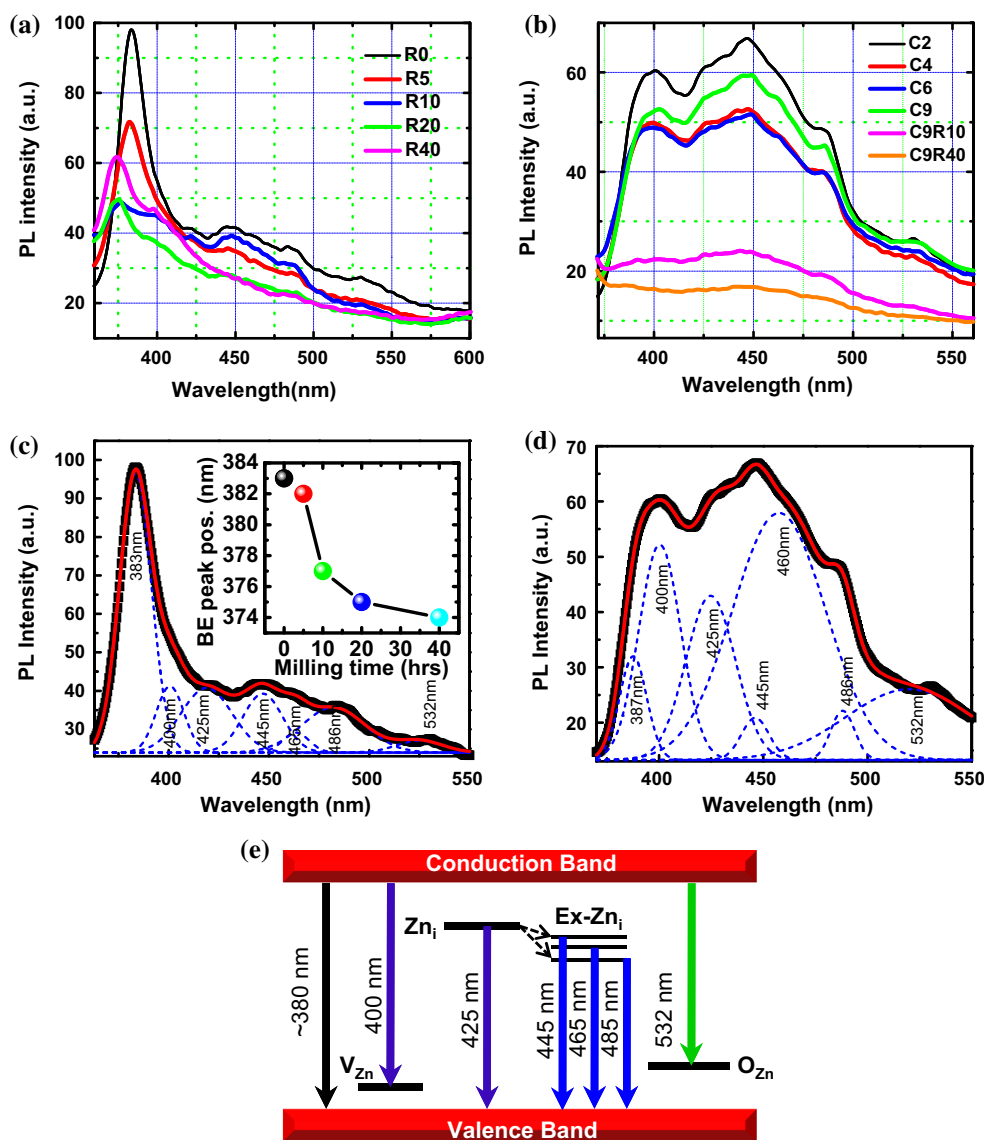
Fig. 5 UV–Vis absorption spectra of room temperature-milled sample and combined cryo- and room temperature-milled samples are shown in **a**, **b**, respectively. *Inset of a* shows a digital photograph of the aqueous dispersion of the sample obtained by 20 h milling at room temperature. **c** Shows the change in absorption peak position with increasing milling time. The variation in particle size as a function of milling time is shown in **d**



In order to investigate the point defects present in the synthesized samples, the RT PL emission spectra of the samples have been measured. These are shown in Fig. 6a, b for the samples obtained by only RT milling and by cryomilling, respectively. For the measurement of PL emission spectra, various excitation wavelengths are used and it has been observed that the PL emission intensity is maximum corresponding to 330 nm excitation wavelength. From the PL emission spectra of the samples obtained by RT milling (Fig. 6a), it can be observed that in addition to a sharp UV emission peak, broad visible PL emission bands are also present in the samples. The presence of visible PL emission band in ZnO appears due to different intrinsic or extrinsic defects. [43–47] Therefore, in order to determine the exact peak positions, the experimentally obtained PL spectra are fitted with the Gaussian fitting and are shown in Fig. 6c, d. From the Gaussian-fitted PL spectra of RT-milled samples, it has been observed that in addition to the sharp UV emission peak appearing due to band-edge (BE) transition, there are six other peaks in the visible region, centred around 400 nm (3.10 eV), 425 nm (2.92 eV), 445 nm (2.79 eV), 465 nm (2.67 eV), 485 nm (2.56 eV) and 532 nm (2.33 eV). No appreciable shift of the visible PL emission peaks is observed with increasing milling time, while the BE emission peak in the UV region is blue shifted from 384 to 374 nm for the samples

obtained by RT milling for 40 h, as shown in the inset of Fig. 5c. This blue shift of the BE emission peak also elucidates the fact that the particle size decreases with increasing milling time. The origin of defect-related visible PL emission spectra in ZnO nanostructures has been studied both experimentally [43–47] and theoretically [47] and different origins for visible PL emissions have been proposed. Following the earlier reports of PL emission in ZnO nanostructures, the observed emission peak at 400 nm (3.10 eV) is assigned to the transition from the conduction band to shallow acceptor levels due to zinc vacancies (V_{Zn}), [42] the blue peak at 425 nm (2.92 eV) is attributed due to transition from zinc interstitial (Zn_i) to the valence band [41], and the series of blue emissions at 445 nm (2.79 eV), 465 nm (2.67 eV) and 485 nm (2.56 eV) are attributed to the transitions from extended Zn_i states to the valence band [47]. These extended Zn_i states can be formed during the milling process according to the defect ionization reaction, as described earlier by Zeng et al. [44]. For such blue emissions, the electrons at first make a transition to the Zn_i state from the conduction band, relax to extended Zn_i states, and finally make a transition to the valence band with blue emissions. The broad PL band appeared in the green region at 532 nm (2.33 eV) is attributed to the transition between conduction band and the energy levels formed with substitution of O at Zn (O_{Zn}) vacancies [46].

Fig. 6 Room temperature PL emission spectra of the samples obtained by room temperature milling and combined cryo and room temperature milling are shown in **a**, and **b**, respectively. For the measurement of PL emission spectra, an excitation wavelength of 330 nm has been used. **c**, **d** shows the Gaussian-fitted PL spectra of the starting material (R0) and the sample obtained by cryomilling (C2), respectively. *Inset of c* shows the position of the band-edge emission peak as a function of milling time for RT-milled samples. **e** Shows a schematic of the energy band diagram



Based on the above discussions, a schematic of energy level diagram showing different transitions responsible for PL emissions is shown in Fig. 6e. Further, from Fig. 5a, it can also be observed that the intensity of both the UV and visible PL emission is quenched in the samples which are obtained after longer milling time, viz. the BE peak is quenched by ~62 % and the defect-related visible PL emission is quenched by ~31 % in 40 h RT-milled sample. From Fig. 6b, it is also found that the intensity of the defect-related visible emission peaks is more than the intensity of the BE emission peak, indicating the presence of more defect states in the samples obtained by cryo and combined cryo and RT milling. Further, both the BE emission and defect-related visible PL emission intensity have been quenched significantly when the cryomilled samples are further milled at room temperatures. As discussed earlier, the wurtzite to cubic phase transformation as

well as the reduction of particle size takes place when the bulk ZnO samples having wurtzite phase are ball milled. As it is well known that the WZ phase shows enhanced PL emission and RS-cubic phase is indirect band gap, the observed PL emission quenching may be associated due to the appearance of cubic ZnO phase or due to the reduction in particle size or both.

Conclusion

Through detailed milling experiments using specially designed temperature controlled mill (KC0), we have explored the effect of pressure, temperature and size on WZ to RS phase transformation of ZnO. Using a combined Cryo and RT milling, we have synthesized and retained cubic phase ZnO nanoparticles of <20 nm at ambient conditions.

Detailed TEM analysis indicates that high defect concentration plays a crucial role in stabilizing high temperature and pressure, cubic RS phase. These phases normally appear reversibly only at high temperature and pressure. A detailed MD simulation supports the role of defects in stabilization process. The UV–Vis absorption spectroscopy of the samples indicates blue shifts in the band-edge absorption indicating the reduction of particle sizes with increasing milling time. The studies of PL emission spectroscopy indicate that in addition to the sharp band-edge emission peak, defect-related visible PL emission peaks are also present in the samples. The observed reduction in emission intensity for both the UV emission and visible emission with increasing milling time has appeared due to the transformation of WZ to RS phase of ZnO.

Acknowledgements The authors would like to acknowledge the electron microscopy facilities available at the Advanced Facility for Microscopy and Microanalysis, Indian Institute of Science (IISc), Bangalore, India. The authors are grateful to UGC-NRCM, IISc, Bangalore for the partial financial support.

Compliance with ethical standards

Conflict of interest The authors declare that they have no conflict of interest.

References

- Ozgun U, Alivov YI, Liu C, Teke A, Reshchikov MA, Dogan S, Avrutin V, Cho SJ, Morkoc H (2005) A comprehensive review of ZnO materials and devices. *J Appl Phys* 98:041301
- Wang ZL (2004) Zinc oxide nanostructures: growth, properties and applications. *J Phys* 16:R829
- Pearnton SJ, Norton DP, Ip K, Heo YW, Steiner T (2005) Recent progress in processing and properties of ZnO. *Prog Mater Sci* 50:293–340
- Decremps F, Datchi F, Saitta AM, Polian A, Pascarelli S, Diccio A, Itie JP, Baudelet F (2003) Local structure of condensed zinc oxide. *Phys Rev B* 68:104101–1041010
- Serrano J, Romero AH, Manjan FJ, Lauck R, Cardona M, Rubio A (2004) Pressure dependence of the lattice dynamics of ZnO: an ab initio approach. *Phys Rev B* 69:94306–94320
- Gerward L, Olsen JS (1995) The high-pressure phase of zincite. *J Synchrotron Radiat* 2:233–235
- Cai J, Chen N (2007) First-principles study of the wurtzite-to-rocksalt phase transition in zinc oxide. *J Phys* 19:266207
- Solozhenko VL, Kurakevych OO, Sokolov PS, Baranov Andrey N (2011) Kinetics of the wurtzite-to-rock-salt phase transformation in ZnO at high pressure. *J Phys Chem A* 115:4354–4358
- Wang S, Fan Z, Koster RS, Fang C, van Huis MA, Yalcin AO, Tichelaar FD, Zandbergen HW, Vlucht TJH (2014) New ab initio based pair potential for accurate simulation of phase transitions in ZnO. *J Phys Chem C* 118:11050–11061
- Desgrenier S (1998) Structural and compressive parameters high-density phases of ZnO. *Phys Rev B* 58:14102–14115
- Decremps F, Datchi F, Saitta AM, Polian A, Pascarelli S, Diccio A, Itie IP, Baudelet F (2003) Local structure of condensed zinc oxide. *Phys Rev B* 68:104101
- Baranov AN, Sokolov PS, Tafeenko VA, Lathe C, Zubavichus YV, Veligzhanin AA, Chukichev MV, Solozhenko VL (2013) Nanocrystallinity as a route to metastable phases: rock salt ZnO. *Chem Mater* 25:1775–1782
- Gao Z, Gu Y, Zhang Y (2010) First-principles studies on the structural transition of ZnO nanowires at high pressure. *J Nanomater* 5:462032–462042
- Kulkarni AJ, Zhou M, Sarasamak K, Limpijumngong S (2006) Novel phase transformation in ZnO nanowires under tensile loading. *Phys Rev Lett* 97:105502
- Jiang Z, Olsen JS, Gerward L, Frost D, Rubie D, Peyronneau J (2000) Structural stability in nanocrystalline ZnO. *Europhys Lett* 50:48–52
- Zhang L, Huang H (2007) Structural transformation of ZnO nanostructures. *Appl Phys Lett* 90:23115–23117
- Dong Z, Zhuravlev KK, Morin SA, Li L, Jin S, Song Y (2012) Pressure-induced structural transformations of ZnO nanowires probed by X-ray diffraction. *J Phys Chem C* 116:2102–2107
- Kotmool K, Bovornratanaraks T, Chakraborty S, Ahuja R (2015) The effect of morphology and confinement on the high-pressure phase transition in ZnO nanostructure. *J Appl Phys* 117:114309–114314
- Wang L, Liu H, Qian J, Yang W, Zhao Y (2012) Structural stability and compressibility study for ZnO nanobelts under high pressure. *J Phys Chem C* 116:2074–2079
- Tiwary CS, Kashyap S, Biswas K, Chattopadhyay K (2013) Synthesis of pure iron magnetic nanoparticles in large quantity. *J Phys D* 46:385001–385005
- Verma A, Biswas K, Tiwary CS, Mondal AK, Chattopadhyay K (2011) Combined Cryo and room-temperature ball milling to produce ultrafine halide crystallites. *Metall Mater Trans A* 42:1127–1137
- Tiwary CS, Verma A, Biswas K, Mondal AK, Chattopadhyay K (2011) Preparation of ultrafine CsCl crystallites by combined cryogenic and room temperature ball milling. *Ceram Int* 37:3677–3686
- Tiwary CS, Saha S, Kumbhakar P, Chattopadhyay K (2014) Observation of combined effect of temperature and pressure on cubic to hexagonal phase transformation in ZnS at the nanoscale. *Cryst Growth Design* 14(9):4240–4246
- Barai K, Tiwary CS, Chattopadhyay PP, Chattopadhyay K (2012) Synthesis of free standing nanocrystalline Cu by ball milling at cryogenic temperature. *Mater Sci Eng A* 558:52–58
- Mohamed FA (2003) A dislocation model for the minimum grain size obtainable by milling. *Acta Mater* 51:4107–4119
- Glushenkov AM, Zhang HZ, Chen Y (2008) Reactive ball milling to produce nanocrystalline ZnO. *Mater Lett* 62:4047–4049
- Ao W, Li J, Yang H, Zhang X, Ma X (2006) Mechanochemical synthesis of zinc oxide nanocrystalline. *Powder Technol* 168:148–151
- Tsuzuki T, McCormick PG (2001) ZnO nanoparticles synthesised by mechanochemical processing. *Scr Mater* 44:1731–1734
- Zhao DS, Zhao M, Jiang Q (2002) Size and temperature dependence of nanodiamond–nanographite transition related with surface stress. *Diam Relat Mater* 11:234–236
- Bate CH, White WB, Roy R (1962) New high-pressure polymorph of zinc oxide. *Science* 137:993
- Gilbert B, Huangs F, Lin Z, Goodell C, Zhang H, Banfield JF (2006) Surface chemistry controls crystallinity of ZnS nanoparticles. *Nano Lett* 6:605–610
- Huang F, Banfield JF (2005) Size-dependent phase transformation kinetics in nanocrystalline ZnS. *J Am Chem Soc* 127:4523–4529
- Li S, Lian JS, Jiang Q (2008) Modeling size and surface effects on ZnS phase selection. *Chem Phys Lett* 455:202–206
- Liang T, Shan TR, Cheng YT, Devine BD, Noordhoek M, Li Y, Lu Z, Phillpot SR, Sinnott SB (2013) Classical atomistic simulations of surfaces and heterogeneous interfaces with the

- charge-optimized many body (COMB) potentials. *Mater Sci Eng* 74:255–279
35. Subramanian AK, Sun CT (2008) Continuum interpretation of virial stress in molecular simulations. *Int J Solid Struct* 45:4340–4346
 36. Stuart SJ, Tutein AB, Harrison JA (2000) A reactive potential for hydrocarbons with intermolecular interactions. *J Chem Phys* 112:6472–6474
 37. Rapaport DC (2004) *The art of molecular dynamics*, 2nd edn. Cambridge publishers, Cambridge, p 90
 38. Chichvarina O, Herng TS, Phuah KC, Xiao W, Bao N, Feng YP, Ding J (2015) Stable zinc-blende ZnO thin films: formation and physical properties. *J Mater Sci* 50:28–33. doi:10.1007/s10853-014-8561-0
 39. Jiang JZ (2004) Phase transformations in nanocrystals. *J Mater Sci* 39:5103–5110. doi:10.1023/B:JMSE.0000039191.87985.c1
 40. Kakazey M, Vlasova M, Dominguez-Patino M, Leon I, Ristic M (2007) Reactionary processes during mechanical treatment of mixtures of ZnO and MnO₂. I. Formation of defects and solid solution. *J Mater Sci* 42:7116–7122. doi:10.1007/s10853-007-1550-9
 41. Chakraborty S, Tiwary CS, Kole AK, Kumbhakar P, Chattopadhyay K (2013) A simple method of synthesis and optical properties of Mn doped ZnO nanocups. *Mater Lett* 91:379–382
 42. Kumbhakar P, Singh D, Tiwary CS, Mitra AK (2008) Chemical synthesis and visible photoluminescence emission from monodispersed ZnO nanoparticles. *Chalcogenide Lett* 5:387–394
 43. Djuricic AB, Leung YH (2006) Optical properties of ZnO nanostructures. *Small* 2:944–961
 44. Zeng H, Duan G, Li Y, Yang S, Xu X, Cai W (2010) Blue Luminescence of ZnO nanoparticles based on non-equilibrium processes: defect origins and emission controls. *Adv Funct Mater* 20:561–572
 45. Fan XM, Lian JS, Zhao L, Liu YH (2005) Single violet luminescence emitted from ZnO films obtained by oxidation of Zn film on quartz glass. *Appl Surf Sci* 252:420–424
 46. Zeng H, Yang S, Xu X, Cai W (2009) Dramatic excitation dependence of strong and stable blue luminescence of ZnO hollow nanoparticles. *Appl Phys Lett* 95:191904–191906
 47. Xu PS, Sun YM, Shi CS, Xu FQ, Pan HB (2003) The electronic structure and spectral properties of ZnO and its defects. *Nucl Instrum Methods Phys Res B* 199:286–290